Research Article Vol. 60, No. 18 / 20 June 2021 / Applied Optics 5335

applied optics

Quantitative theory of integrating sphere throughput: comparison with experiments

Adam Francis,[1,3] Chhayly Tang,[1] and Eric C. Le Ru[1,2,*]

[1]School of Chemical and Physical Sciences, Victoria University of Wellington, PO Box 600, Wellington 6140, New Zealand
[2]The MacDiarmid Institute for Advanced Materials and Nanotechnology, Victoria University of Wellington, PO Box 600, Wellington 6140, New Zealand
[3]e-mail: adamfrancis02@gmail.com
*Corresponding author: eric.leru@vuw.ac.nz

Received 20 April 2021; revised 17 May 2021; accepted 17 May 2021; posted 18 May 2021 (Doc. ID 428450); published 14 June 2021

We present a rigorous approach for measuring the throughput of an integrating sphere, from which the so-called sphere multiplier M can be derived. The critical ingredients of this approach are: (i) the transmitted power is measured at the base of an integrating port to avoid non-ideal port effects associated with reflections on the port wall; (ii) to implement this last point, optical fibers are used for light collection, providing a well-defined collection area and numerical aperture; (iii) the angular-dependent fiber throughput and detector sensitivity are determined experimentally and accounted for. We demonstrate in particular that a more realistic theory, accounting for the propagation of skew rays through the fiber, is needed to quantitatively model the fiber effect on the measured sphere throughput. We show experimentally that failure to fulfill these three points produces erroneous results, by as much as 50%. With an accurate experimentally derived sphere multiplier, agreement with theory is then obtained only if realistic ports (with non-zero reflectivity) are assumed. This provides experimental evidence for recent theoretical predictions of the importance of realistic ports [Tang *et al.*, Appl. Opt. 57, 1581 (2018)]. Using the same experimental techniques, we also present clear experimental proof of two other predictions from that study: that the angular distribution exiting the port is strongly altered and that the overall port transmittivity is drastically reduced for high aspect ratio ports. This work will provide a solid basis for future quantitative measurements of absolute throughput and for further developments of the theory of integrating spheres.

https://doi.org/10.1364/AO.428450

1. INTRODUCTION

Integrating spheres are spherical cavities whose inner walls are coated with a highly reflecting and diffusing material. Typically a polytetrafluoroethylene (PFTE) material such as Spectralon is used for the visible range. They also typically contain ports, i.e., holes on the cavity, where light can be sent inside or detected, or where a sample can be placed. They are commonly used in two main configurations [1,2]: with a light source inside the sphere for spectrophotometry (to quantify total power or quantum yield) [3,4] or with a sample on the cavity wall (sample port) for the measurement of the total reflectance of a sample (so-called diffuse reflectance) [5–7]. Other applications include their use as gas sensors [8–11] or for liquid sample absorbance measurements [12–19]. The theory of integrating spheres was laid out more than 50 years ago [20,21] and further refined in the context of diffuse reflectance to account, for example, for a flat sample or a limited field of view [22–27]. Central to this theory is the concept of the sphere multiplier M, which relates the flux Φ [W/m^2] received by any area of the sphere walls to the power P_0 [W] incident into the sphere (of radius a_S):

$$\Phi = M\frac{P_0}{4\pi a_S^2}. \tag{1}$$

Note that M also quantifies the average number of reflections a photon experiences inside the sphere before being absorbed by the wall or escaping through a port. This flux, or the corresponding sphere multiplier, will naturally depend on the presence of a reflecting/scattering/absorbing sample inside or on the wall of the sphere. But for the empty sphere, M is related only to the reflectivity of the cavity walls ρ and the areas A_i of the ports (relative to total cavity wall area). It is common to define the port fraction for each port as $f_i = A_i/(4\pi a_S^2)$ and the total port fraction as $f = \sum_i f_i$. M can then be derived to be [1,20,27]

$$M = \frac{\rho}{1-\rho(1-f)}. \tag{2}$$

This standard expression can also be generalized [21] to the case where the sphere is composed of $N+1$ regions, each of fractional area f_i and reflectivity ρ_i ($i = 0 \ldots N$), and where region 0 corresponds to where the incident light first hits the wall (for example, the sample in diffuse reflectance measurements):

$$M = \frac{\rho_0}{1 - \rho\left(1 - \sum_{i=0}^{N} f_i\right) - \sum_{i=0}^{N} f_i \rho_i}. \quad (3)$$

This expression reduces to the earlier one when $\rho_0 = \rho$ and $\rho_i = 0$ $(i \geq 1)$. Note that this expression relates only to an empty sphere, which is the subject of this work. A number of extensions have been derived in the context of diffuse reflectance to account, for example, for the presence of a flat sample at a port or non-Lambertian effects [20,22–25].

Despite the fact that these expressions are widely used to account for the absolute throughput in integrating spheres, we have not found any reports where they are validated experimentally. This is partly due to the fact that an absolute throughput measurement is in general not necessary for many applications where a ratio of throughput is measured, for example, a sample on the wall against a reference sample or the empty sphere to extract the reflection/absorption/scattering properties of the sample. Other studies have focused on how the sphere multiplier is affected by external parameters such as temperature [28], but this again does not require a correct absolute measurement. Yet, the experimental validation of absolute throughput in an empty sphere should be simple: M can in principle be estimated by measuring the total power in and total power out through a port of known radius. We suspect such a study has not been reported simply because it does not work. For example, we did this simple measurement in one of our spheres and inferred $M_{\text{exp}} \approx 30$ at 650 nm. Knowing that $f \approx 0.0046$, this would imply from Eq. (2) that $\rho \approx 0.97$, which seems quite far off from the expected value for Spectralon (above 0.99) [29]. Such large discrepancies cannot be attributed solely to experimental problems such as the angular dependence of the power meter or the cleanliness of the sphere wall. It is also in general not possible to compare the results to an independent direct measurement of the sphere wall reflectivity, as such absolute measurements, although possible, are difficult and involve specialist equipment or reflectance standards.

We have recently shown [30] using Monte Carlo (MC) ray-tracing simulations that light propagation in ports and the associated reflections off the port walls can result in a substantial fraction being reflected back into the sphere. In other words, most realistic ports have a non-zero, and sometimes large, reflectivity. According to Eq. (3), this translates to large changes in the predicted sphere multiplier M (or the sphere reflectivity ρ derived from it). Another consequence of non-zero port reflectivity is that the port transmission is reduced, which will affect the value of M inferred from a power measurement through a port. Reference [30] also showed that the angular profile exiting a port could also be modified, further affecting the power if measured through a fiber, as commonly done.

With these improvements in the theory, it should now be possible to investigate its validity experimentally. It is therefore the purpose of this paper to demonstrate the possible quantitative agreement between theory and experimental measurements of sphere throughput. To this end, we have developed a reliable procedure for measuring sphere throughput using an optical fiber for detection, which provides the advantage of a well-defined collection area (with core radius a_{fib}) and numerical aperture (NA). The standard integrating sphere theory predicts a sphere throughput for fiber detection [1,30]:

$$Q_{\text{port}} = \frac{P_{\text{port}}}{P_0} = M f_{\text{port}} \text{NA}^2, \quad (4)$$

where $f_{\text{port}} = a_{\text{port}}^2/(4a_S^2)$ is the fiber core fraction. This arises from: (i) a Lambertian illumination at the input and (ii) an ideal transmission through the fiber up to the angle corresponding to the fiber NA. We will show that the first assumption is valid only at the port base because of real-port effects, and the second is not accurate enough, as it does not account for skew rays in the fiber. To avoid these issues, we instead developed a method for careful characterization of the angle-dependent fiber and detector throughput. This knowledge can then be applied to deduce the correct sphere multiplier [which is different, by 50% in some cases, from that obtained from applying Eq. (4)]. The fiber imaging method also allows us to experimentally demonstrate the predictions in Ref. [30] that the angular profile is modified by the port and more intense for an on-axis ray than the Lambertian distribution at the entrance of the port. Finally, we also evidence experimentally the strong port aspect ratio dependence of the overall port transmission, as also predicted in Ref. [30].

2. METHODS

A. Experimental

A single integrating sphere of inner radius $a_S = 25$ mm, depicted in Fig. 1(a), was used for all measurements. It has two identical deep and narrow cylindrical ports of radius $a_{\text{port}} = 1.6$ mm and height $h_{\text{port}} = 16.3$ mm, whose axes are parallel to a sphere diameter but offset by 17.68 mm. The third port is wider ($a_{\text{port}} = 3.5$ mm) and shorter ($h_{\text{port}} = 12.5$ mm) and aligned with a sphere diameter. Note that this specific

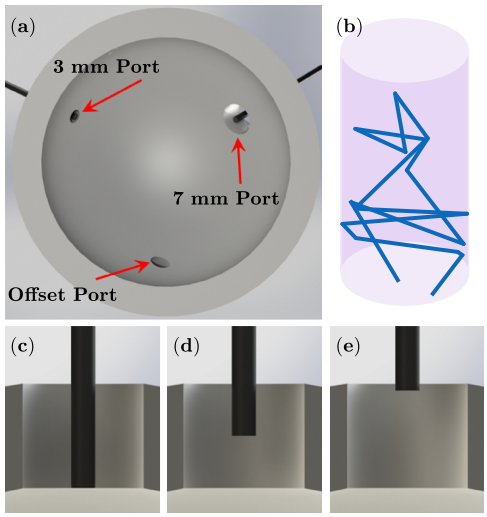

Fig. 1. (a) Internal view of the integrating sphere showing port positions and dimensions. When measuring the 7 mm and 3.1 mm ports, the off-axis and 7 mm ports were used as illumination ports, respectively. (b) Example of a random photon trajectory inside the port (here returning to the sphere) as derived from the Monte Carlo simulations. (c)–(e) Schematics showing possible positions of the optical fiber inside the 7 mm port. For accurate throughput measurements, the fiber is placed at the port base (c) avoiding real-port effects in collection. Positions such as (d) and (e) can be used to investigate real-port effects as a function of port height.

configuration was not created purposely for this study but for applications in absorption spectroscopy of liquids [17–19]; it can nevertheless be used to support our arguments. The two off-axis ports were not used for the measurements, but need to be accounted for when modeling the sphere multiplier. For the purpose of this work, another on-axis port was created, with radius $a_{\text{port}} = 1.5$ mm and height $h_{\text{port}} = 20$ mm.

Monochromatic low-power (∼5 mW) laser diodes, either green (532 nm) or red (674.2 nm), were used for excitation to avoid any complication associated with the wavelength dependence of the integrating sphere or optical components. Light was directed through either the large 7 mm port or one of the 3.1 mm off-axis ports. In the latter case, a lens was used to reduce the beam diameter (normally a few millimeters) to ensure it was not clipping the port walls. Light is collected with an optical fiber at the base of the port [flush with the inner sphere surface; Fig. 1(c)] or at precisely measured heights away inside the ports [Figs. 1(d) and 1(e)] to mimic the effects of ports of different heights. For the latter, the integrating cavity was placed on a micrometer stage while the proximal fiber end (fiber end inside the sphere) was fixed in place. This allowed for the measurement of multiple port heights with 1 mm intervals and an error of ±0.2 mm. Two fibers of different NAs and sizes were used to investigate angular-dependent effects, see full specifications in Table 1. Both fibers were purchased from Thorlabs, and one end was left flat cleaved with no connector, which meant it could be easily inserted into narrow ports. Multimode fibers with relatively large core sizes were used to maximize throughput. Both fibers were of relatively short length, and under the experimental conditions, we could not observe any losses associated with the fiber bend radius used.

For throughput measurements, the light exiting the fibers was measured with a butt-coupled Thorlabs PM100D power meter. The power entering the sphere was measured with the same power meter, either butt-coupled to the laser (for the 7 mm port) or after the focusing lens (off-axis port). In all cases, the laser power was averaged over a 30 s integration time. The ratio of the two power measurements (before the sphere and after the fiber) after dark subtraction gives the total system throughput. No baffles were used, as the combination of the port placement relative to the input port and the fiber NA were such that the first reflection was not collected by the fiber. MC simulations predict that there is a small dependence of throughput on the exact position of the fiber in the port. This is, however, negligible unless the fiber face is significantly off center in a large port. In all experiments, we have nevertheless endeavored to center the fiber face in the port, which then leaves a gap between the outer fiber shield and the port wall (except in the 3 mm port where this is negligible). In our calculation, it is assumed that light entering this gap is lost, which we believe is a reasonable approximation given the outer shield of our fiber is a black plastic.

The angular profile at the fiber exit was measured by imaging it on a CMOS array. As this involves a number of additional technical and theoretical developments, it is discussed separately in the result section.

Table 1. Properties of the Two Thorlabs Fibers Used in This Work

NA	Core Size [mm]	Length [m]	Name
0.22	0.60	1.0	FG600AEA
0.39	1.00	1.5	FT1000UMT

B. Monte Carlo Simulations

MC ray-tracing calculations [12,31] were carried out to predict the properties of real cylindrical ports as explained in Ref. [30]. These consist of following the trajectory of a photon as it undergoes stochastic reflection/absorption events when intersecting the port wall [see illustration in Fig. 1(b)]. From these, the probability of escape τ_{port} (port transmittivity), of return ρ_{port} (port reflectivity), and of absorption α_{port} were computed. Note that

$$\tau_{\text{port}} + \rho_{\text{port}} + \alpha_{\text{port}} = 1. \tag{5}$$

Those parameters depend primarily on the port aspect ratio defined as $\xi = h_{\text{port}}/(2a_{\text{port}})$, with a_{port} and h_{port} the port radius and height, respectively, and, to a lesser extent, wall reflectivity ρ_w. In the general case, the port wall reflectivity ρ_w may be different from the sphere reflectivity ρ, but unless the port or sphere has been soiled, one can expect them to be similar. We have used $\rho_w = 0.993$ for these calculations, but changing it to $\rho_w = 0.99$, for example, had a negligible effect on the results. Note that MC simulations were adapted to take into account the off-axis geometry of the two offset ports.

For an integrating sphere configuration with port fractions f_i and reflectivity of each port ρ_i, we can then deduce the effective port fraction:

$$\bar{f} = \sum f_i(1 - \rho_i). \tag{6}$$

Assuming a value for the sphere reflectivity ρ, we may then deduce M from [see Eq. (3)]

$$M = \frac{\rho}{1 - \rho(1 - \bar{f})}. \tag{7}$$

Conversely, if M is obtained experimentally, then ρ can be deduced. Note that in the thin-port limit ($\xi = 0$ or $h_{\text{port}} = 0$), the port reflectivity is zero, and this equation reduces to Eq. (2).

3. MEASURING THE ANGLE-DEPENDENT THROUGHPUT OF AN OPTICAL FIBER

To determine the angular-dependent throughput of the fiber, we first need a well-defined illumination at its entrance. For this, we place it in the 3 mm port of the integrating sphere at a port height of zero (flush with the internal wall) [Fig. 1(c)]. This ensures that the illumination at the fiber entrance is Lambertian with radiant intensity proportional to $\cos\theta$. The illumination of the sphere is through the 7 mm port.

A. Fiber Output Imaging

To characterize the light output at the exit, we place it at a distance L from the CMOS array detector of a Fujifilm X-A20 camera [see Fig. 2(a)]. The CMOS detector is 23.6 × 15.6 mm in size with a pixel size of 4.8 × 4.8 μm (2456 × 1639 pixels each for red, blue, and twice green). This detector was placed on a micrometer stage to allow for accurate control of the fiber-detector distance L. The link between the intensity profile on

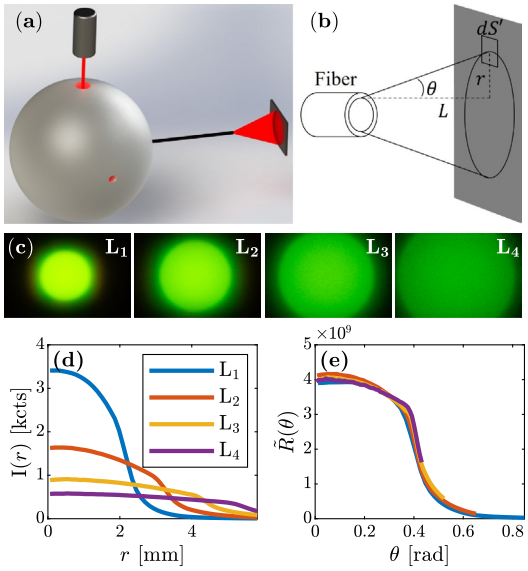

Fig. 2. (a), (b) Schematics of the fiber profiling experiment using a CMOS sensor to image the fiber output. (c) Example raw CMOS images of the fiber output measured at increasing distances $L_i = L_1 + (i-1)\Delta L$ ($\Delta L = 5$ mm) from the fiber exit. From each image, the radially symmetric irradiance profile $I_i(r)$ is extracted and shown in (d). From these, $L_1 = 10.3$ mm is inferred as described in the text, and the corresponding fiber profiles $\tilde{R}_i(\theta)$ are derived from Eq. (10) and shown in (e).

the CMOS array and the angular distribution exiting the fiber can be established as follows.

First, since L is much larger than the fiber core size, we may approximate the fiber exit as a point source. We also assume that the distribution is axially symmetric and therefore defined by a radiant intensity [W/sr] $R(\theta)$. Note that at the fiber entrance, we have a Lambertian illumination characterized by a radiant intensity $R_{\text{in}}(\theta) = I_0 \cos\theta$ or equivalently a probability distribution $p_{\text{in}}(\theta) = \sin(2\theta)$. Similarly, at the fiber exit, we have $R(\theta)$ or $p(\theta) \propto R(\theta)\sin\theta$.

The power [W] received on a surface dS' on the sensor at a distance r from the axis [see Fig. 2(b)] is then given by $dP = R(\theta)d\Omega$, where

$$d\Omega = \frac{dS'\cos\theta}{(L/\cos\theta)^2}. \tag{8}$$

The pixel irradiance [W/m^2] is therefore

$$I(r) = \frac{dP}{dS'} = \eta(\theta)\frac{R(\theta)\cos^3\theta}{L^2}, \tag{9}$$

where we have introduced the angular-dependent detector efficiency $\eta(\theta)$. Together with $r = L\tan\theta$, this expression allows us to derive the angular fiber profile $\tilde{R}(\theta) = \eta(\theta)R(\theta)$ from the intensity pattern $I(r)$ on the sensor as

$$\tilde{R}(\theta) = \frac{L^2 I(L\tan\theta)}{\cos^3\theta}. \tag{10}$$

What is measured on the CMOS sensor is the irradiance [W/m^2] at each pixel position I_i. The raw CMOS images are used to avoid any post-processing being applied, and a dark image is subtracted. Example images are shown in Fig. 2(c), which confirms the axial symmetry of the fiber profile. From such images, the center is first found by taking the weighted centroid, and virtual rings of radius 25 pixels wide are drawn around the center (each of radius $25n$, $n = 1, 2, \ldots$). By averaging I_i for each ring, we obtain the irradiance $I(p_n)$ as a function of pixel distance from center $p_n = 12.5 + 25(n-1)$. This distance in pixel (p) is converted in millimeters (r) by multiplying by $23.6/2456 \approx 9.6$ μm (spacing between pixels). The irradiance profiles measured at four different distances L (each 5 mm apart), corresponding to the raw images in Fig. 2(c), are plotted in Fig. 2(d) for the NA 0.39 fiber. As L increases, the center irradiance decreases, and the image becomes more spread out.

In principle, measurement at a single L is sufficient to extract $\tilde{R}(\theta)$ from Eq. (10), but we here used four equally spaced L for a number of reasons: (i) it allows us to detect problems associated with sensor saturation (more likely at short L) or with the image being cropped or too weak compared to background (more likely at large L); (ii) it checks the validity of the point source assumption (it would create more error at short L); and (iii) it means that we do not have to rely on an absolute measurement of L, which can be difficult because of proprietary sensor coatings. For the latter point, we instead accurately measure the spacing between each measured L: $\Delta L = 5$ mm in our case, and $L_2 = L_1 + \Delta L$. From Eq. (10), we then see that $L_1^2 I_1(L_1 x) = L_2^2 I_2(L_2 x)$ for all x (we have set $x \equiv \tan\theta$), or equivalently,

$$I_2\left(\frac{y}{\beta_{12}}\right) = \beta_{12}^2 I_1(y), \quad \beta_{12} \equiv \frac{L_1}{L_2}. \tag{11}$$

For a given (measured) $I_1(r)$ and $I_2(r)$, we can therefore deduce β_{12} from a one-parameter nonlinear least-square fit of Eq. (11). From it, we then deduce L_1 and L_2 from

$$L_1 = \frac{\beta_{12}}{1-\beta_{12}}\Delta L, \quad L_2 = L_1 + \Delta L. \tag{12}$$

For the example in Fig. 2, we deduce $\beta_{12} = 0.67$ and $L_1 = 10.3$ mm. For the method to be self-consistent, the resulting $\tilde{R}_i(\theta)$ derived from Eq. (10) for each $L_i = L_1 + (i-1)\Delta L (i = 1 \ldots 4)$ should be the same, which is indeed the case within experimental uncertainties, as shown in Fig. 2(e). We can do this for all pairs of L, and we obtain very similar $\tilde{R}(\theta)$ in all cases, which we average to get a single measured $\tilde{R}(\theta)$. A more direct method is to enforce all pairwise conditions $L_i^2 I_i(L_i x) = L_j^2 I_j(L_j x)$ in a one-parameter (L_1) least-square fit. This global fit method gives results similar to the first method. The latter is preferred, as it allows us to detect possible problematic measurements (for example, affected by saturation).

B. Detector Angular Dependence

To characterize the fiber output $R(\theta)$, we still need to correct for the detector efficiency $\eta(\theta)$. CMOS arrays are known to have a strong angle-dependent efficiency, which can be measured with a collimated beam incident on the sensor placed on a rotation stage [32,33]. Example images for this experiment are shown as insets in Fig. 3(a). As all pixels are irradiated at the same

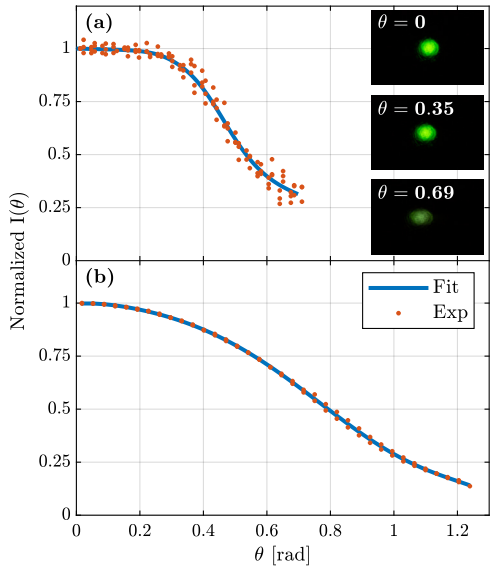

Fig. 3. (a) Angular response of the CMOS sensor $\eta(\theta)$ obtained from imaging a collimated beam for different angles between the beam and sensor. Example raw CMOS images are shown as insets. A spline fit is used to smooth this response (blue line). Note that the response was measured for both negative and positive angles, and was found to be symmetric. (b) Angular response of the power meter, η_{PM} (normalized to one at $\theta = 0$).

incidence angle, the efficiency is simply proportional to the integrated dark-corrected intensity. The resulting $\eta(\theta)$, normalized such that $\eta(0) = 1$, is shown in Fig. 3(a). A spline fit is used to smooth this response to avoid introducing noise. This then allows us to correct the measured $\tilde{R}(\theta)$ and deduce the radiant intensity at the fiber exit from $R(\theta) = \tilde{R}(\theta)/\eta(\theta)$. A similar measurement was performed for red excitation (674 nm), and a much more pronounced angular dependence was found, with η down to less than 20% at angles of $\theta = 0.36$ only. This makes fiber profiling at larger angles very difficult, and red excitation is therefore not suited for such measurements. All measurements presented in this paper will therefore be with green (532 nm) excitation.

Finally, a similar measurement was carried out to characterize the angle-dependent response η_{PM} of the power meter (used for sphere throughput measurements), shown in Fig. 3(b).

4. QUANTIFYING FIBER THROUGHPUT

For any quantitative measurement of integrating sphere throughput, it is paramount to carefully characterize the detector parameters: surface area, NA, and any angular dependence. The latter can be particularly problematic for large NA detection. To capture all the light coming out of a port, a full NA = 1 detection is in principle needed, which is difficult to implement. To overcome this problem, a simple common approach is to use an optical fiber to collect the light from the port and couple it into the detector. The main advantages are that the fiber has a well-defined collection area (core area) and NA, and since the NA is relatively small, it may be argued that the effect of the detector angular dependence becomes negligible (we will show that this is in fact wrong). In the standard theory of integrating spheres [1], a fiber of given NA is assumed to fully transmit all rays reaching its core with an angle-to-axis θ smaller than the critical fiber angle $\theta_{\mathrm{NA}} = a\sin(\mathrm{NA})$. For a Lambertian distribution at its entrance, with an angular probability distribution $p(\theta) = \sin(2\theta)$, this results in a fiber throughput of $Q^L_{\mathrm{fib}} = \mathrm{NA}^2$.

We here argue and will show experimentally that this simple approximation is not suitable to quantitative estimates for several reasons. First, the simple fiber model implicitly assumes that all rays are meridional (passing through the fiber center). To take into account the effect of other rays, known as skew rays, a more general theory must be used [34,35]. We summarize in the appendix the more relevant aspects. The main effect of skew rays is that rays with an angle larger than θ_{NA} can be transmitted through the fiber. This results in an additional tail in the transmittivity $T(\theta)$ for $\theta > \theta_{\mathrm{NA}}$, and in the case of Lambertian illumination, the overall transmission is larger than NA^2 by as much as 50% (see Appendix A). Skew rays must therefore be taken into account for any quantitative interpretation of sphere throughput measurement using fiber optics. Second, in-coupling at the fiber entrance and out-coupling at the fiber exit are unlikely to be perfect, notably because of possible reflection at the air/fiber core interface. This can be easily accounted for with the angle-dependent Fresnel reflection coefficient (averaging over polarization)

$$R(\theta) = \frac{1}{2}\left[\frac{\cos\theta - n_F\cos\theta_z}{\cos\theta + n_F\cos\theta_z} + \frac{n_F\cos\theta - \cos\theta_z}{n_F\cos\theta + \cos\theta_z}\right], \quad (13)$$

where $\sin\theta = n_F\sin\theta_z$. n_F is the fiber core refractive index, θ is the incidence angle outside the fiber, and θ_z is the refracted angle inside the fiber core. Accounting for both in- and out-coupling, the transmission is then $T_{\mathrm{IO}}(\theta) = (1 - R(\theta))^2$. $T_{\mathrm{IO}}(\theta)$ is approximately constant for small angles (of the order of 0.93 for a typical n_F of 1.46), but then decreases at larger angles, which are not negligible given the skew ray contribution and the Lambertian probability $p(\theta) = \sin(2\theta)$ peaking at $\theta \approx 0.7$. Another possible source of imperfections is bending losses: any bend in the fiber could result in further departure between theoretical and real fiber throughput. This will particularly affect angles close to the critical angle θ_{NA}. Only one small-curvature 90° bend was present in most of our experiments. When changing the radius of curvature, we did not observe any noticeable changes to the transmitted power, so this effect is likely negligible in our case. A potential additional loss mechanism is optical absorption in the fiber; however, for short fibers in the visible (less than a few meters, as used in our experiments), this is typically negligible. Finally, real fibers also have cladding, and cladding modes may be present and enhance the transmission at some angles.

It is clear that at the very least, skew rays and in-/out-coupling must be accounted for in any quantitative study. But even then, other effects such as cladding modes may still result in a discrepancy between theory and practice. A more accurate approach is therefore to experimentally measure the fiber transmittivity $T(\theta)$. As explained in the previous section, this can be achieved by imaging the fiber output onto a sensor array at different distances from the output face for a Lambertian illumination at the fiber entrance. By comparing the exit radiant intensity

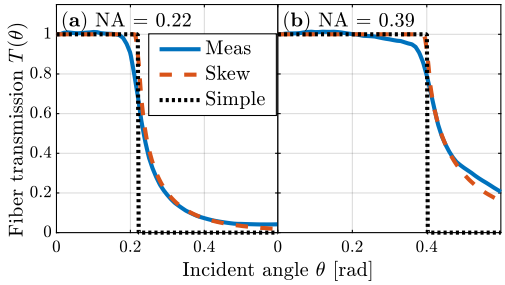

Fig. 4. Transmittivity $T(\theta)$ of the (a) 0.22 NA and (b) 0.39 NA fibers. Four measurements are shown for each fiber along with the theoretical meridional throughput (simple model) and the skew ray models.

to that at the entrance, we obtain $T(\theta)$ for the fiber up to a scaling factor. The scaling factor can be measured by a single throughput measurement with a laser, but we may also assume that $T(\theta = 0) = 1$, as these rays should not be affected by other factors. Note that we here define $T(\theta)$ as the internal transmittivity of the fiber (ignoring in-/out-coupling), and the overall transmittivity is therefore $T_{\mathrm{IO}}(\theta)\, T(\theta)$.

Following this approach, we measured $T(\theta)$ for the two fibers of NAs 0.22 and 0.39, and this is summarized in Fig. 4. These are compared to the ideal fiber theory and to the improved theory accounting for skew rays. Note that θ denotes the external angle, not the internal angle (after refraction at the entrance face). In the ideal theory of Ref. [1] (ignoring skew rays), the transmittivity is simply

$$T_{\mathrm{ideal}}(\theta) = \begin{cases} 1 \text{ if} \theta \le \theta_{\mathrm{NA}} \\ 0 \text{ if} \theta > \theta_{\mathrm{NA}} \end{cases}. \tag{14}$$

In contrast, we clearly observe transmission beyond the critical angle, with a similar dependence as predicted from the skew ray theory. The agreement is, however, not exact, in particular, for $\theta \approx \theta_{\mathrm{NA}}$. Such small discrepancies are difficult to account for in the theory because the details of the fiber outer structure are not available from the manufacturers.

Once the transmittivity is determined, the overall fiber throughput for a given probability distribution of incidence angle at the fiber entrance is

$$Q_{\mathrm{fib}} = \int_0^{\pi/2} p(\theta)\, T_{\mathrm{IO}}(\theta)\, T(\theta) \mathrm{d}\theta. \tag{15}$$

The derived Q^L_{fib} for a Lambertian incidence are summarized in Table 2 for the two fibers investigated in this work and different assumptions on $T(\theta)$. It is clear that errors as large as 50% in throughput may arise from using the ideal fiber model. In contrast, the skew ray theory predicts throughput comparable to those inferred experimentally. In fact, the experimentally derived throughput is affected by the larger uncertainties in the experimental transmittivity at large angles (above 0.6 rad). It may be more accurate to extrapolate the experimental data above 0.6 rad using the skew ray theory results (see last row in the table). In any case, Table 2 and Fig. 4 clearly demonstrate the importance of carefully characterizing fiber throughput and that the ideal fiber theory is inadequate. The experimentally derived transmittivity, or in our case the one obtained from the skew ray theory, must instead be used to infer accurate throughputs.

Finally, it should be noted that for sphere throughput measurements, the angle-dependent transmittivity of the fiber is convoluted with the angle-dependent sensitivity of the power meter, and the throughput of the combined collection apparatus is then given by

$$Q_{\mathrm{fib+PM}} = \int_0^{\pi/2} p(\theta)\, T_{\mathrm{IO}}(\theta)\, T(\theta) \eta_{\mathrm{PM}}(\theta) \mathrm{d}\theta, \tag{16}$$

where $\eta_{\mathrm{PM}}(\theta)$ was measured in the previous section. For Lambertian illumination, $p(\theta) = \sin(2\theta)$, and the derived $Q_{\mathrm{fib+PM}}$ are also summarized in Table 2. The pattern is roughly similar to that observed for the fiber-only throughputs, but we do observe that the power meter response has a non-negligible effect, especially on the larger NA fiber. This further highlights the importance of careful characterization of the angular dependence in collection (both fiber and detector).

5. ACCURATE MEASUREMENT OF THE SPHERE MULTIPLIER

With the fiber collection carefully accounted for, we are now in a position to obtain rigorous measurements of the sphere multiplier. To avoid any influence of the port transmission and angular redistribution (which will be the subject of the next sections), we here focus on measurements where the fiber entrance is placed at the base of the port at the inner sphere surface [see Fig. 1(c)]. The sphere throughput is then given by

$$Q_{\mathrm{sphere}} = M \frac{a^2_{\mathrm{fib}}}{4a^2_S} Q^L_{\mathrm{fib+PM}}. \tag{17}$$

The second term is equivalent to the "port fraction," here the ratio of fiber core to inner sphere surface areas. $Q^L_{\mathrm{fib+PM}}$ accounts for the fiber and detector response for Lambertian illumination (which is the case at the base of the port) and was determined experimentally in the previous section. The sphere multiplier M can then be determined from a measurement of the sphere throughput. The results of such measurements are summarized in Table 3. First, we see that the derived M is relatively large, of the order of 90. Also, the M derived from two measurements with different fibers is identical, which provides further support to the result. In contrast, if we had assumed the ideal fiber transmission $Q^L_{\mathrm{fib}} = \mathrm{NA}^2$, then the resulting M_{direct} differ by about 15% for the two different fibers, which further supports the importance of careful fiber characterization.

Such large M's have not been previously reported, probably partly because they seem incompatible with the standard theoretical expression [Eq. (2)]. Indeed, the total port fraction for our sphere is $f = 7.8 \times 10^{-3}$, so the resulting M_{direct} of 122 would correspond to a wall reflectivity of $\rho = 0.9996$, much larger than the highest reported reflectivity of PTFE [36], of the order of 0.994. (It is important to note that in these measurements of ρ, the relevant quantity is $1 - \rho$; therefore, a value of 0.9996 is wrong by an order of magnitude.) This contradiction is not as pronounced but still remains with our improved measurement of $M = 90.2$.

Table 2. Normalized Throughput for Lambertian Incidence for the Fiber, Q^L_{fib}/NA^2, and for Full Collection System (Fiber and Power Meter), Q^L_{fib+PM}/NA^{2a}

	Fiber 1 NA 0.22 Core 0.6 mm		Fiber 2 NA 0.39 Core 1 mm	
	Fib	Fib+PM	Fib	Fib+PM
Ideal	0.94	0.93	0.94	0.88
Skew rays	1.55	1.45	1.5	1.27
Experimental	1.58	1.46	1.43	1.25
Exp.+skew	1.48	1.38	1.47	1.24

[a]The fiber transmittivity is taken from the (i) ideal fiber theory, (ii) skew ray theory, (iii) experimental measurement, and (iv) experimental values up to $\theta = 0.45$ rad extrapolated with the skew ray values for $\theta > 0.45$ rad (where the experiment is more uncertain).

Table 3. Experimentally Derived M at $\lambda = 532$ nm for 0.22 NA and 0.39 NA Fibers, and Main Parameters Used: Fiber NA, Core Radius a_{fib}, Lambertian Throughput Q^L_{fib+PM} (from Table 2), and Measured Sphere Throughput Q_{sphere} [M Calculated Using Eq. (17)][a]

NA	a_{fib}	$\frac{Q^L_{fib+PM}}{NA^2}$	Q_{sphere}	M	M_{direct}
0.22	0.3	1.458	2.27×10^{-4}	89.2	130.1
0.39	0.5	1.248	1.73×10^{-3}	91.1	113.7
Ave				**90.2**	**121.9**

[a]For comparison, we also show M_{direct}, computed directly from the common assumption $Q^L_{fib+PM} = NA^2$.

These problems were highlighted theoretically in Ref. [30] and attributed to the non-negligible port reflectivities. These can be calculated using MC simulations as summarized in Table 4 (note that these were also tabulated in Ref. [30], but do not apply to our ports 2 and 3, as their axes do not cross the center of the sphere). In the case of our sphere, even the widest port (7 mm diameter, 11 mm high) has a predicted large reflectivity of $\rho_P = 0.59$. The effective sphere port fraction, $\bar{f} = \sum_i (1 - \rho_i) f_i$, is then dramatically reduced, down to $\bar{f} = 2.5 \times 10^{-3}$. Together with the measured $M = 90.2$, we then deduced a sphere wall reflectivity of $\rho = 0.9915$. This is in the expected range for a PTFE sphere that has been used for a few months (ours had been used for about six months). We note that without the fiber transmission correction, we had $M_{direct} = 122$, and the derived ρ would have been 0.9943, which would be above the maximum expected for a brand new/clean sphere and is therefore unrealistic.

6. FURTHER EXPERIMENTAL EVIDENCE FOR REAL-PORT EFFECTS

The non-zero reflectivity of real ports was evidenced in the previous section indirectly through its effect on M, but the corresponding reduced port transmittivity can in principle be observed more directly in a throughput measurement. Our measurement of the intensity profile at the fiber exit also allows us to test experimentally another prediction of Ref. [30]: the port-induced angular redistribution. For this, we use the large NA fiber to maximize the range of measured angles, and collect

Table 4. Port Properties and Calculated Reflectivities and Transmittivities Using MC Simulation with $\rho = 0.993$ (Exact Value of ρ Has Only Minor Influence)[a]

	Diameter [mm]	Height [mm]	$f_P \times 10^{-3}$	ρ_P	$\bar{f}_P \times 10^{-3}$
Port 1	7.0	11.0	4.90	0.59	2.0
Ports 2 and 3	3.2	16.3	1.45	0.83	0.24
Port 4	3	23.0	0.23	0.83	0.04
Total			**7.80**		**2.50**

[a]The effective port fraction is $\bar{f}_P = (1 - \rho_P) f_P$. For ports 2 and 3, the port axis does not go through the sphere center but half a sphere radius from it.

the light from the integrating sphere at various depths inside the port [see Figs. 1(c)–1(e)]. At a distance h from the inner sphere surface, the situation is equivalent to a port of height h or, to use the notation of Ref. [30], a port aspect ratio $\xi = h/2a_P$. $\xi = h = 0$ corresponds to the base of the port (thin-port limit), discussed earlier. The angular profile at the fiber exit is then imaged on a CMOS array and analyzed as described in Section 3 to derive the radiant intensity at the port exit $R_{exit}(\theta)$. As evident from the raw images [Fig. 5(a)], there is a clear angular redistribution with a more localized pattern as the port height increases. This is also evident in the combined port+fiber transmittivity inferred from these images [see Fig. 5(b)]. To eliminate the effect of the transmittivity of the fiber, we can also normalize $R_{exit}(\theta, \xi)$ for a given port height to that measured at $h = 0$ (studied in the previous section), $R_{exit}(\theta, \xi = 0)$. This is shown in Fig. 5(c) and again highlights the angular redistribution effect, here independently of the fiber transmission.

These experimental results are compared to MC ray-tracing predictions (following Ref. [30]) [see dashed lines in Figs. 5(b) and 5(c)]. We see that there is a good qualitative, and even semi-quantitative, agreement. In particular, the angle at which the transmission starts to differ from the $\xi = 0$ case is correctly predicted by theory. As the angle increases further, the intensity drop is, however, overestimated in the ray-tracing predictions.

The other, arguably more obvious, real-port effect is the reduced port transmittivity. This can be measured in the same configurations as just described, with a power meter at the end of the fiber. The theoretical sphere throughput takes the form

$$Q_{sphere(\xi)} = M \frac{a^2_{fib}}{4a^2_S} Q_{fib+PM}(\xi), \tag{18}$$

where $Q_{fib+PM}(\xi)$ is given by Eq. (16), this time with a modified $p(\xi, \theta)$, as a result of transmission through the port. The transmittivity of the fiber $T(\theta)$ and power meter response $\eta_{PM}(\theta)$ are unchanged and were characterized in Section 4. For this experiment, we moved the fiber in steps of 2 mm from the top exit of the port, $z = 0$, down to the bottom (just inside the sphere), $z = h_{port}$. We summarize our results in Fig. 6. We first compare the throughput dependence on port height for the two centered ports (3 mm and 7 mm), measured with the same NA 0.39 fiber [Fig. 6(a)]. As expected, the throughput decreases with increasing port height as a result of reduced port transmittivity, and the effect is more pronounced in the narrow port. This is understandable, since as explained in Ref. [30], the most important parameter is the aspect ratio ξ. In fact, when plotted against ξ, Fig. 6(b), the two plots are then approximately

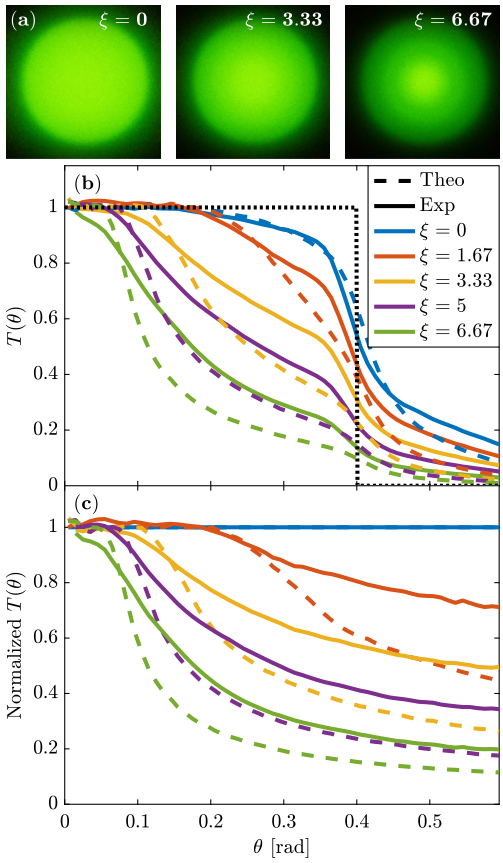

Fig. 5. Measurement of the port+fiber angular-dependent transmittivity as a function of port height h_{port}, or equivalently, aspect ratio $\xi = h_{\text{port}}/(2a_{\text{port}})$, for the 3 mm port and NA 0.39 fiber. The overall port+fiber transmittivities $T(\theta)$ (normalized to $T(0) = 1$) are shown in (b) for different ξ. Example raw CMOS images from which these curves are extracted are shown in (a). (c) Same data normalized to $T(\theta, \xi = 0)$, to remove any influence of the fiber. All dashed lines are ray-tracing predictions.

superimposed. These results are also compared to ray-tracing predictions, and we again observe qualitative agreement, but the predicted transmittivity is again underestimated at higher aspect ratios.

We believe the discrepancy with theory observed in both angular dependence and throughput could be related to the non-ideal-Lambertian diffuse reflection, which can result in a higher probability of scattering at very large angles (above 75°–80°). This effect has been evidenced experimentally [36,37]. For a long and narrow port, this results in a higher probability of rays being scattered along or close to the port axis and therefore of exiting the port without further hitting the wall. This could explain simply why the experimental results show higher transmission than predicted from the ideal Lambertian reflection. This suggests that including non-Lambertian reflection in the ray-tracing theory may be necessary to accurately predict real-port effects in long or narrow ports.

7. CONCLUSION

We have developed a rigorous experimental protocol to measure the throughput of integrating spheres and derive their sphere

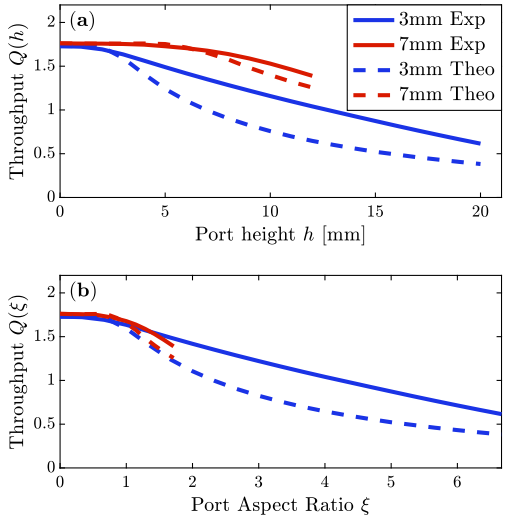

Fig. 6. Overall sphere+port+fiber+power meter throughput as a function of (a) port height or (b) port aspect ratio for the two centered ports. Dashed lines are ray-tracing predictions.

multiplier. This has allowed us to demonstrate experimentally previously predicted real-port effects: non-zero port reflectivity, reduced port transmittivity, and angular redistribution. Because of these, it is crucial to measure the sphere throughput at the base of the port. A convenient way to achieve this is with optical fibers. In this case, we have shown that the standard theory of fiber collection results in a large error in the sphere multiplier. We have shown that this is due to the non-negligible contribution of skew rays. Our proposed method to measure fiber transmission overcomes this problem, and we have shown that the result agrees closely with an improved theory including skew rays. The derived sphere multipliers, obtained after such improvements and a careful characterization of the detector angular dependence, are of the order of 100, much larger than typically thought. Such values do appear in agreement with the expected sphere wall reflectivity, but only if the non-zero port reflectivities are accounted for.

This study therefore provides a comprehensive, quantitative, and self-consistent experimental and theoretical picture of integrating sphere absolute throughput. Reassuringly, our conclusions should not strongly affect applications where relative throughputs are measured to infer sample properties, as errors related to fiber or port transmittivity should equally affect the sample and reference. Nevertheless, we believe this study will provide a solid basis for future quantitative measurements of absolute throughput and for further developments of the theory of integrating spheres.

APPENDIX A: SKEW RAYS IN OPTICAL FIBERS

The common description of optical fiber transmission implicitly assumes that all rays are meridional (passing through the fiber center). To take into account the effect of other rays, known as skew rays, a more general theory must be used [34,35]. We summarize below the more relevant aspects; refer to, e.g., Ref. [35] for full details. Note that the skew ray theory

summarized here assumes a relatively simple step-index fiber. Some real fibers may have a graded index, or more steps.

A general skew ray direction (inside the fiber) is characterized by its angle with the fiber axis, denoted θ_z following Ref. [35], and a second angle θ_ϕ related to the skewness. Both angles are conserved at each reflection inside the fiber. Following Ref. [35], we defined α as the angle between the incident ray and the fiber surface normal (relevant to refraction/total internal reflection (TIR):

$$\cos\alpha = \sin\theta_z \sin\theta_\phi. \tag{A1}$$

Note that for meridional rays, $\theta_\phi = \pi/2$, and α and θ_z are complementary angles ($\alpha + \theta_z = \pi/2$). According to Snell's law, TIR inside the core of refractive index n_F should occur for $\alpha \geq \alpha_c$ and refraction for $\alpha < \alpha_c$ with

$$n_F \sin\theta_c = \mathrm{NA} \text{ and } \sin\alpha_c = \cos\theta_c, \text{ i.e. } \alpha_c = \pi/2 - \theta_c. \tag{A2}$$

To take into account skew rays, we can therefore simply replace the transmission condition $\theta_z < \theta_c$ by $\alpha > \alpha_c$, which we will call the basic skew ray model. Note that this requires defining all the properties of the fiber: refractive index n_F, NA, core radius a_F (although the dependence on the latter is small), and the full properties of incoming rays (position and direction) to determine θ_ϕ. For a given ray entering at (x_0, y_0, z_0) on the fiber face with direction unit vector (u_x, u_y, u_z), we have

$$\begin{aligned}
\cos\theta_i &= u_z, \\
\sin\theta_z &= \sin(\theta_i)/n_F, \\
\cos\theta_\phi &= \frac{1}{a_F}\sqrt{x_0^2 + y_0^2 - \frac{(x_0 u_x + y_0 u_y)^2}{(u_x^2 + u_y^2)}}.
\end{aligned} \tag{A3}$$

Assuming a Lambertian illumination at the entrance of the fiber, we can then calculate the full transmission of the fiber as a function of external angle θ. This is illustrated in Fig. 4 for the two fibers used in this work. It is clear that the skew rays dramatically affect the fiber transmittivity. A more elaborate skew ray model also accounts for the modification of Snell's law because of the curved interface, which may allow some otherwise totally internally reflected rays to tunnel out [35]. It can be shown that only rays with $\theta_z < \theta_c$ are strictly bound by TIR. Rays with $\alpha > \alpha_c$ and $\theta_z > \theta_c$ are called leaky rays or tunneling rays. They would be undergoing TIR on a flat surface, but because of the curvature, they have a small probability of not reflecting. The exact transmission probabilities of leaky rays can be computed following the treatment in Ref. [35] (not reproduced here because of the complications) and the fiber transmission derived for a given entrance illumination. Including those adds many complications to the theory (and would require detailed knowledge of the cladding structure), but as a rule of thumb, the changes are small for short fibers as used in this work.

Funding. MacDiarmid Institute for Advanced Materials and Nanotechnology (PhD Scholarship); Victoria University of Wellington (PhD Scholarship).

Disclosures. The authors declare no conflicts of interest.

Data Availability. Data underlying the results presented in this paper are not publicly available at this time but may be obtained from the authors upon reasonable request.

REFERENCES

1. K. F. Carr, "Integrating sphere theory and applications part I: integrating sphere theory and design," Surf. Coat. Int. **80**, 380–385 (1997).
2. K. F. Carr, "Integrating sphere theory and applications part II: integrating sphere applications," Surf. Coat. Int. **80**, 485–490 (1997).
3. K. Suzuki, A. Kobayashi, S. Kaneko, K. Takehira, T. Yoshihara, H. Ishida, Y. Shiina, S. Oishi, and S. Tobita, "Reevaluation of absolute luminescence quantum yields of standard solutions using a spectrometer with an integrating sphere and a back-thinned CCD detector," Phys. Chem. Chem. Phys. **11**, 9850–9860 (2009).
4. H. Ishida, S. Tobita, Y. Hasegawa, R. Katoh, and K. Nozaki, "Recent advances in instrumentation for absolute emission quantum yield measurements," Coordin. Chem. Rev. **254**, 2449–2458 (2010).
5. W. W. Wendlandt and H. G. Hecht, *Reflectance Spectroscopy* (Interscience, 1966).
6. W. Erb, "Requirements for reflection standards and the measurement of their reflection values," Appl. Opt. **14**, 493–499 (1975).
7. W. Richter and W. Erb, "Accurate diffuse reflection measurements in the infrared spectral range," Appl. Opt. **26**, 4620–4624 (1987).
8. P. Elterman, "Integrating cavity spectroscopy," Appl. Opt. **9**, 2140–2142 (1970).
9. E. S. Fry, G. W. Kattawar, and R. M. Pope, "Integrating cavity absorption meter," Appl. Opt. **31**, 2055–2065 (1992).
10. J. T. O. Kirk, "Modeling the performance of an integrating-cavity absorption meter: theory and calculations for a spherical cavity," Appl. Opt. **34**, 4397–4408 (1995).
11. M. T. Cone, J. A. Musser, E. Figueroa, J. D. Mason, and E. S. Fry, "Diffuse reflecting material for integrating cavity spectroscopy, including ring-down spectroscopy," Appl. Opt. **54**, 334–346 (2015).
12. N. B. Nelson and B. B. Prézelin, "Calibration of an integrating sphere for determining the absorption coefficient of scattering suspensions," Appl. Opt. **32**, 6710–6717 (1993).
13. M. Babin and D. Stramski, "Light absorption by aquatic particles in the near-IR spectral region," Limnol. Oceanogr. **47**, 911–915 (2002).
14. T. Jávorfi, J. Erostyák, J. Gál, A. Buzády, L. Menczel, G. Garab, and K. R. Naqvi, "Quantitative spectrophotometry using integrating cavities," J. Photochem. Photobiol. B **82**, 127–131 (2006).
15. A. K. Gaigalas, H.-J. He, and L. Wang, "Measurement of absorption and scattering with an integrating sphere detector: application to microalgae," J. Res. Natl. Inst. Stand. Technol. **114**, 69–81 (2009).
16. Y. Villanueva, C. Veenstra, and W. Steenbergen, "Measuring absorption coefficient of scattering liquids using a tube inside an integrating sphere," Appl. Opt. **55**, 3030–3038 (2016).
17. B. L. Darby, B. Auguié, M. Meyer, A. E. Pantoja, and E. C. Le Ru, "Modified optical absorption of molecules on metallic nanoparticles at sub-monolayer coverage," Nat. Photonics **10**, 40–45 (2016).
18. J. Grand, B. Auguié, and E. C. Le Ru, "Combined extinction and absorption UV–visible spectroscopy as a method for revealing shape imperfections of metallic nanoparticles," Anal. Chem. **91**, 14639–14648 (2019).
19. A. Djorović, S. J. Oldenburg, J. Grand, and E. C. Le Ru, "Extinction-to-absorption ratio for sensitive determination of the size and dielectric function of gold nanoparticles," ACS Nano **14**, 17597–17605 (2020).
20. J. A. Jacquez and H. F. Kuppenheim, "Theory of the integrating sphere," J. Opt. Soc. Am. **45**, 460–470 (1955).
21. D. G. Goebel, "Generalized integrating-sphere theory," Appl. Opt. **6**, 125–128 (1967).
22. B. J. Hisdal, "Reflectance of perfect diffuse and specular samples in the integrating sphere," J. Opt. Soc. Am. **55**, 1122–1125 (1965).
23. B. J. Hisdal, "Reflectance of nonperfect surfaces in the integrating sphere," J. Opt. Soc. Am. **55**, 1255–1260 (1965).
24. H. L. Tardy, "Flat-sample and limited-field effects in integrating sphere measurements," J. Opt. Soc. Am. A **5**, 241–245 (1988).
25. H. L. Tardy, "Matrix method for integrating-sphere calculations," J. Opt. Soc. Am. A **8**, 1411–1418 (1991).

26. M. A. Bukhshtab, "Method of determination of small scattering coefficients," J. Appl. Spectrosc. **46**, 523–528 (1987).
27. M. A. Bukhshtab, *Photometry, Radiometry, and Measurements of Optical Losses*, 2nd ed., Springer Series in Optical Sciences, (Springer, 2019).
28. C. P. Ball, A. P. Levick, E. R. Woolliams, P. D. Green, M. R. Dury, R. Winkler, A. J. Deadman, N. P. Fox, and M. D. King, "Effect of polytetrafluoroethylene (PTFE) phase transition at 19°C on the use of Spectralon as a reference standard for reflectance," Appl. Opt. **52**, 4806–4812 (2013).
29. Labsphere, "Spectralon diffuse reflectance material [online]," 2019, https://www.labsphere.com.
30. C. Tang, M. Meyer, B. L. Darby, B. Auguié, and E. C. Le Ru, "Realistic ports in integrating spheres: reflectance, transmittance, and angular redirection," Appl. Opt. **57**, 1581–1588 (2018).
31. B. Liu, Y. Yuan, Z.-Y. Yu, X. Huang, and H.-P. Tan, "Numerical investigation of measurement error of the integrating sphere based on the Monte-Carlo method," Infrared Physics and Technology **79**, 121–127 (2016).
32. P. B. Catrysse, X. Liu, and A. E. Gamal, "QE reduction due to pixel vignetting in CMOS image sensors," Proc. SPIE **3965**, 420–430 (2000).
33. P. B. Catrysse and B. A. Wandell, "Optical efficiency of image sensor pixels," J. Opt. Soc. Am. A **19**, 1610–1620 (2002).
34. A. Cozannet and M. Treheux, "Skew rays in optical fibers," Appl. Opt. **14**, 1345–1350 (1975).
35. A. W. Snyder and J. Love, *Optical Waveguide Theory* (Chapman and Hall, 1983).
36. V. R. Weidner and J. J. Hsia, "Reflection properties of pressed polytetrafluoroethylene powder," J. Opt. Soc. Am. **71**, 856–861 (1981).
37. J. M. Sanz, C. Extremiana, and J. M. Saiz, "Comprehensive polarimetric analysis of Spectralon white reflectance standard in a wide visible range," Appl. Opt. **52**, 6051–6062 (2013).